Air Force Institute of Technology

AFIT Scholar

Faculty Publications

10-2021

Solar Cell BRDF Measurement and Modeling with Out-of-plane Data

Todd V. Small
Air Force Institute of Technology

Samuel D. Butler
Air Force Institute of Technology

Michael A. Marciniak
Air Force Institute of Technology

Follow this and additional works at: https://scholar.afit.edu/facpub

Part of the Optics Commons

Recommended Citation

Todd V. Small, Samuel D. Butler, and Michael A. Marciniak, "Solar cell BRDF measurement and modeling with out-of-plane data," Opt. Express 29, 35501-35515 (2021).

This Article is brought to you for free and open access by AFIT Scholar. It has been accepted for inclusion in Faculty Publications by an authorized administrator of AFIT Scholar. For more information, please contact AFIT.ENWL.Repository@us.af.mil.

Research Article | Vol. 29, No. 22 / 25 Oct 2021 / *Optics Express* 35501

Solar cell BRDF measurement and modeling with out-of-plane data

Todd V. Small,[1,*] **Samuel D. Butler,**[1] **and Michael A. Marciniak**[1]

Department of Engineering Physics, Air Force Institute of Technology (AFIT), 2950 Hobson Way, Wright-Patterson, AFB, OH 45433, USA
[*]*todd.small@afit.edu*

Abstract: In this work, a CCD-augmented complete angle scatter instrument (CASI) with a visible red laser source was used to measure the BRDF of a commercially available solar cell designed for small satellites, simultaneously capturing both in-plane and out-of-plane data with high angular resolution surrounding the specular direction. The measurements exhibited three distinct scatter features: a central specular peak, an offset specular peak, and a diffraction pattern. The two peaks were caused by different material surfaces with slightly different normal directions, and the diffraction pattern arose from periodically-spaced metal conducting bars running in one direction across the solar cell surface. The diffraction pattern measurements were verified in-plane with an original single-pixel CASI detector and then used to inform the creation of a single closed-form BRDF model capable of describing the out-of-plane features. Both specular peaks were modeled using a traditional microfacet formulation, but the offset peak model implemented a rotation of the incident and scatter directions to account for the difference in surface normal direction. The diffraction pattern–which is not typically described with microfacet models–was described based on Fraunhofer diffraction through two rectangular stripes, adjusted in terms of microfacet coordinates. Parameters for the model were chosen manually, based largely on physical material properties when possible, rather than using optimized fitting algorithms. Model results were compared to the measurements by using the same CCD pixel scatter coordinates. Qualitatively, the model successfully replicated the observed features, and quantitatively, the modeled peak values agree with the measurements within an order of magnitude.

1. Introduction

The bi-directional reflectance distribution function (BRDF) defines the spatial distribution of light reflected from a material surface [1]. Material BRDFs can be modeled using a diverse range of mathematical formulations, but due to a desire for both computational efficiency and radiometric accuracy, remote sensing applications commonly rely on closed-form isotropic microfacet models [2–4]. However, due to their simplifying assumptions, such models are typically unable to describe out-of-plane BRDF features from materials with more complex or anisotropic surface characteristics.

This work uses a commercially available solar cell designed for satellites as an example material which possesses complex surface structure. Following a brief discussion in Sec. 2 of pertinent BRDF measurement and modeling background, Sec. 3 presents in-plane and out-of-plane solar cell BRDF measurements surrounding the specular direction, collected using a Complete Angle Scatter Instrument (CASI) augmented with a charge-coupled device (CCD) detector. In addition to the central specular peak, the measurements display a second offset specular peak caused by a surface with a different normal direction, as well as a highly-directional diffraction pattern caused by metal conducting bars periodically spaced along one dimension of the solar cell surface – neither of which are typically included in closed-form BRDF models. The diffraction pattern measurements are validated in Sec. 3.3 by comparison with the original CASI detector.

Section 4 presents the construction of a closed-form BRDF model with three terms capable of describing each of the three prominently measured features, including their out-of-plane

#440190 https://doi.org/10.1364/OE.440190
Journal © 2021 Received 15 Aug 2021; revised 4 Oct 2021; accepted 4 Oct 2021; published 14 Oct 2021

characteristics. One term models a central specular peak using a standard microfacet formulation; a second term models an offset specular peak with a similar formulation but rotates the incident and scatter directions to account for the difference in surface normal direction; and a third term models a diffraction pattern by reformulating a known closed-form solution from Fourier optics in terms of microfacet and scatter coordinates. Section 4.4 combines each term and compares the model results with measurements, showing that the model successfully replicates each feature.

2. Background

Formally, the BRDF is the ratio of scattered radiance to incident irradiance [5], generally written

$$f_r(\boldsymbol{\hat{\omega}_i}, \boldsymbol{\hat{\omega}_s}, \lambda) = \frac{dL_s(\boldsymbol{\hat{\omega}_i}, \boldsymbol{\hat{\omega}_s}, \lambda)}{dE_i(\boldsymbol{\hat{\omega}_i}, \lambda)}. \tag{1}$$

In this expression, λ is the wavelength, and $\boldsymbol{\hat{\omega}_i}$ and $\boldsymbol{\hat{\omega}_s}$ represent incident and scattered directions, respectively, which are often written in spherical coordinates (θ_i, ϕ_i) and (θ_s, ϕ_s). Scatter directions within the plane of incidence (in-plane) are defined relative to the incident direction by $\phi_i = \phi_s$ or $\phi_i = \phi_s + \pi$. Scatter directions with other ϕ_s values, then, are located somewhere outside the plane of incidence (out-of-plane).

In analyzing bulk scatter in general terms, there are two hemispheres of interest, which are collectively referred to by the Bidirectional Scatter Distribution Function (BSDF). By convention, $\theta_s = 0$ refers to the overall surface normal direction. In this convention, $\theta_s \leq \pi/2$ corresponds to the BRDF, while $\pi/2 < \theta_s \leq \pi$ corresponds to the Bidirectional Transmission Distribution Function (BTDF). Since a solar cell is negligibly transmissive and is the subject of this work, only the BRDF ($\theta_s \leq \pi/2$) will be considered in this paper when referring to scatter. In other words, the BSDF is the sum of the BRDF and BTDF in general, although in this case only the BRDF contributes a non-negligible value.

The BRDF is commonly used in scene generation via the Rendering Equation, [6]

$$L_s(\hat{\omega}_s, \lambda) = L_e(\hat{\omega}_s, \lambda) + \int_{\Omega_+} f_r(\hat{\omega}_i, \hat{\omega}_s, \lambda) L_i(\hat{\omega}_i, \lambda) \cos\theta_i \, d\hat{\omega}_i, \tag{2}$$

where L_s is the total scattered radiance, L_i is the incident radiance, L_e is the self-emitted radiance, and Ω_+ represents the incident hemisphere. The BRDF is thus crucial in obtaining the total radiance scattered off an object. In this work, as can be imagined when viewing an object in space (such as a satellite) from a far off distance (such as from the Earth), high spatial resolution is required. As a tradeoff, in this work (as with many high fidelity BRDF model papers) we limit ourselves to a single wavelength, 632.8 nm; other wavelength measurements are saved for future work. We further assume L_e is negligible at this wavelength, since the self-emission even from a blackbody at satellite temperatures at visible wavelengths is negligible compared to the scattered radiance; self-emission is saved for future work at infrared wavelengths.

Fundamentally, microfacet models assume geometric optics and describe the material surface as comprised of many very small specularly-reflecting facets, whose orientations relative to the overall surface normal are described within a microfacet distribution function [7]. The general underlying form for most microfacet BRDF models can be written [8]

$$f_r(\boldsymbol{\hat{\omega}_i}, \boldsymbol{\hat{\omega}_s}) = \rho_s D(\boldsymbol{\hat{\omega}_h}) F(\boldsymbol{\hat{\omega}_d}) G(\boldsymbol{\hat{\omega}_i}, \boldsymbol{\hat{\omega}_s}) \sigma(\theta_i, \theta_s) + \rho_v V(\boldsymbol{\hat{\omega}_i}, \boldsymbol{\hat{\omega}_s}) + \frac{\rho_d}{\pi}, \tag{3}$$

which consists of three terms. The primary term with weight ρ_s is the specular term, which contains the microfacet distribution function D, a Fresnel reflectance function F, a shadowing and obscuration function G, and a cross-section conversion σ. The second term weighted ρ_v is the volumetric term, which accounts for additional scattering features such as subsurface particle

scattering, although in practice, many microfacet models ignore this contribution [8]. The third term weighted ρ_d is a constant Lambertian factor.

The microfacet distribution and Fresnel functions are often more conveniently expressed in terms of microfacet coordinates [9]. Here, $\hat{\omega}_h$ represents the microfacet normal direction – or equivalently the half-angle direction located directly between the incident and scattered directions. Similarly, $\hat{\omega}_d$ is simply the incident direction expressed relative to the microfacet normal direction $\hat{\omega}_h$ rather than the overall surface normal. The conversion from scatter to microfacet coordinates is

$$\hat{\omega}_h = \frac{\hat{\omega}_i + \hat{\omega}_s}{||\hat{\omega}_i + \hat{\omega}_s||} \qquad \hat{\omega}_d = \mathbb{R}_y(-\theta_h)\mathbb{R}_z(-\phi_h)\hat{\omega}_i, \tag{4}$$

where the generic notation $\mathbb{R}_a(\gamma)$ represents a rotation about the a-axis by the angle γ.

Due to the fundamental assumption of geometric optics, microfacet models almost exclusively ignore wavelength-dependent features, and so λ does not appear anywhere in Eq. (3). Phenomena such as diffraction are rooted in the wave nature of light, but BRDF models which include wave optics, such as the Modified Beckmann-Kirchhoff [10] or Generalized Harvey-Shack [11,12] models, are much more computationally intensive and often do not possess closed-form solutions. Based on comparisons between microfacet and wave optics formulations, the Q polarization factor can be used to replace F, G, and σ within Eq. (3) [13]. The modification

$$f_r(\hat{\omega}_i, \hat{\omega}_s) = \rho_s D(\hat{\omega}_h)\frac{Q(n, \hat{\omega}_i, \hat{\omega}_s)}{2(\cos\theta_i + \cos\theta_s)^2} + \frac{\rho_d}{\pi} \tag{5}$$

improves microfacet model performance at grazing angles [14].

The vast majority of BRDF measurement research assumes isotropic material surface characteristics [15,16], which tends to inform models with isotropic microfacet distribution functions. For example, satellite observation simulations traditionally incorporate isotropic solar cell BRDFs, usually matching the form of Eq. (3) [17–21], but sometimes simply assuming Lambertian reflectance [22]. However, because solar cells generally possess complex surface structures involving coverglass, metal conducting bars, and photovoltaic layers, such models are not able to incorporate out-of-plane or wavelength-dependent scatter features. Especially since solar cells often represent one of the largest external surface areas on many satellites, the omission of out-of-plane information has the potential to degrade agreement between overall satellite observations and simulations. Our novel CCD-augmented CASI provides a method for simultaneously obtaining both in-plane and out-of-plane BRDF data with high angular resolution, particularly surrounding the specular direction, where each pixel measures flux reflected into a unique scatter direction [23,24].

3. Solar cell BRDF measurements

The solar cell obtained for this study consists of periodically-spaced metal conducting bars mounted atop triple-junction photovoltaic absorption layers with an epoxy-mounted coverglass. Figure 1 provides a general schematic of the solar cell's layered material structure. According to production specifications, the metal bars are approximately 10 μm wide and spaced approximately 800 μm apart, running in one direction along the solar cell surface. Using alignment, calibration, and measurement techniques established in previous work for the CCD-augmented CASI [23,24], the solar cell was mounted onto the material sample stage, and specular measurements were captured for incident angles of 20°, 40°, and 60° using a 632.8 nm helium neon (HeNe) laser source. For this particular solar cell, the top photovoltaic layer is InGaP, which is typically responsible for ultraviolet and visible absorption below about 650 nm [25]. Even with the beam focused at the pixel array, the sample's illumination spot was large enough to encompass multiple metal bars. Due to occlusion of the source by the detector, 20° was selected as the lower limit for

incident angle; due to material sample mount grazing limitations, 60° was selected as the upper limit; and 40° provided an incident angle in between.

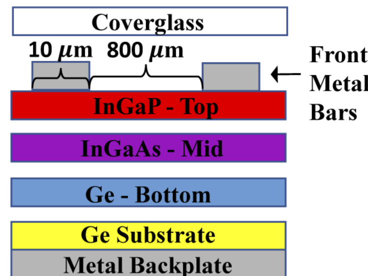

Fig. 1. Cross-sectional illustration of the solar cell's material layer structure. At 632.8 nm used in this work, the light penetrating beyond the top InGaP layer is negligible. The drawing is not to scale.

3.1. Metal bars oriented in-plane

Figure 2 shows BRDF measurement results from one particular illumination spot when the solar cell is mounted with the metal bars aligned with the in-plane (horizontal) direction. Figures 2(a) and 2(c) display the entire pixel array of BRDF measurements for $\theta_i = 20°$ and $\theta_i = 60°$, respectively, which simultaneously include both in-plane and out-of-plane data centered on the specular direction.

Even qualitatively, three distinct scatter features are distinguishable: 1) one specular peak centered in the frame, 2) a second specular peak offset from the first, and 3) a vertical diffraction pattern oriented in the out-of-plane direction. Figures 2(b) and 2(d) extract BRDF values from the pixel columns running vertically (out-of-plane) through the center of each specular peak in Figs. 2(a) and 2(c). At both incident angles, the diffraction pattern signal is well above any detector and artifact noise levels [26], and therefore caused by solar cell surface features. However, for larger θ_i, as in Fig. 2(c), the diffraction pattern begins to curve noticeably.

Measurement uncertainty was calculated using previously defined methodology, which identified neutral density (ND) filter uncertainty as the largest contributor [26]. The measurement for $\theta_i = 20°$ required ND filters with a combined optical density (OD) of $OD_m = 3.3$, while the measurement for $\theta_i = 60°$ required an increase to $OD_m = 4.0$ in order to handle the higher scatter flux at that angle. For $OD_m = 3.3$, none of the stacked ND filters matched those used for the beam signature, and so the worst-case ND filter uncertainty based on published tolerances was 59.3%. For $OD_m = 4.0$, however, the same 4.0 OD filter was also used in the beam signature, and so the worst-case ND filter uncertainty was 14.0%.

It is important to note that unlike many other uncertainty contributions, ND filter uncertainty affects each pixel's BRDF measurement uniformly, and so does not impact the relative shape of the BRDF. When ND filter uncertainty is omitted from the overall uncertainty calculation, the average relative uncertainty considering all other contributions across all pixels for the $\theta_i = 20°$ measurement in Fig. 2(a) is only 4.00% with a standard deviation of 0.29%. For the $\theta_i = 60°$ measurement in Fig. 2(c), the average relative uncertainty is 6.42% with a standard deviation of 0.24%.

3.2. Metal bars oriented out-of-plane

Fourier optics teaches that diffraction through rectangular apertures results in far field irradiance patterns with sinc^2 spacing between high-frequency peaks [27]. More details involving specific diffraction model construction and numerical parameter selection are given in Secs. 4.3 and

Research Article | Vol. 29, No. 22 / 25 Oct 2021 / Optics Express 35505
Optics EXPRESS

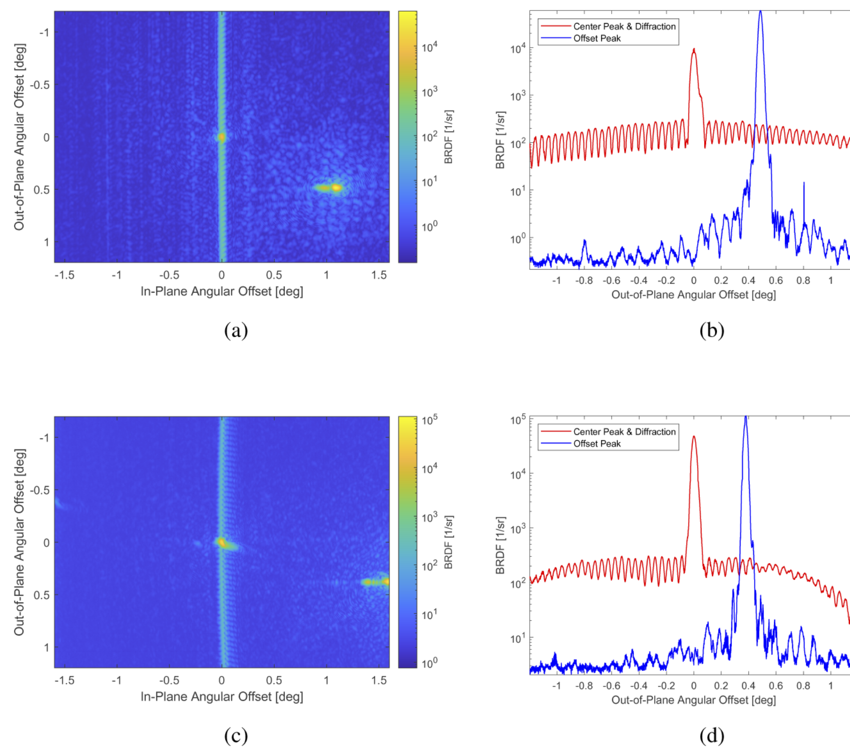

Fig. 2. Solar cell BRDF measurement data using a 15 mW red HeNe laser source with metal conducting bars oriented in-plane, where $\theta_i = 20°$ in (a) and (b), and $\theta_i = 60°$ in (c) and (d). The full CCD pixel arrays in (a) and (c) capture three distinct scatter features, which include a central specular peak, an offset specular peak, and a diffraction pattern. The pixel column readings through the center of each peak, plotted in (b) and (d), show that each feature lies well above the noise floor.

4.4, but the high-frequency pattern displayed in Fig. 2 corresponds very well to the diffraction expected through rectangular apertures whose dimensions match the solar cell's conducting bars. It is thus possible to deduce that the diffraction pattern noticeable in the BRDF measurement is caused by the solar cell's periodically spaced metal bars.

As a result, changing the orientation of the bars by rotating the solar cell about its surface normal should cause a corresponding change in diffraction pattern orientation. Figure 3 compares measurements at $\theta_i = 40°$ with the metal bars oriented approximately 45° out-of-plane in (a) and fully out-of-plane in (b). The illumination spot on the solar cell is the same for both cases, although slightly different than the spot used in Fig. 2. As expected, the diffraction pattern orientation changes with solar cell orientation.

No matter how the solar cell is oriented, one specular peak always appears aligned with the center of the diffraction pattern. This peak is plausibly linked to the photovoltaic material beneath the metal bars, indicating that these two materials have very similar surface normal directions. The second specular peak, however, is very clearly offset from the first peak. Its apparent location rotates about the center peak as the solar cell rotates, and even shifts location slightly as the illumination spot changes. In addition, when a white sheet of paper is slowly advanced from the CCD to the sample stage (taking advantage of the visible laser source), the apparent spacing between the two peaks gradually shrinks. The combination of these behaviors indicates that the second specular peak is caused by another material whose surface normal points in a slightly

Optics EXPRESS

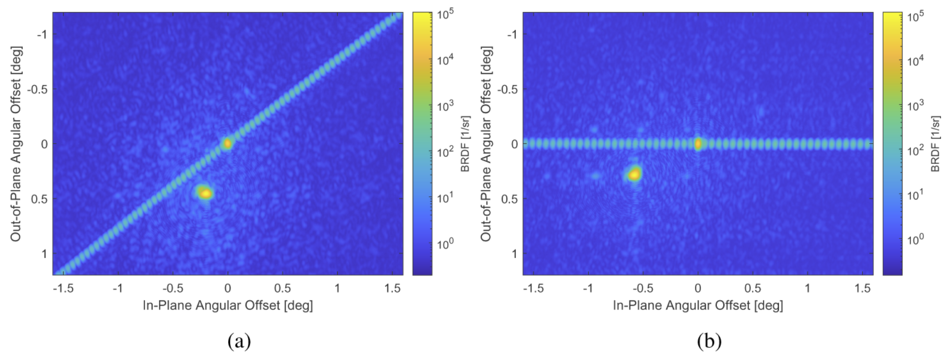

Fig. 3. Solar cell BRDF measurement data using a 15 mW red HeNe laser source and $\theta_i = 40°$, with the metal conducting bars oriented 45° out-of-plane in (a) and fully out-of-plane in (b). Both the diffraction pattern and the offset specular peak rotate about the center specular peak along with the solar cell.

different direction. The coverglass for this particular solar cell was manually affixed with epoxy, with slightly uneven or offset applications possible, making it a plausible candidate for the cause of the second peak.

With each feature plausibly arising from scatter or reflection from a different material surface, it follows that the peaks of each feature do not necessarily share the same magnitude, because each material may have different properties affecting the BRDF, including index of refraction. For instance, if the center peak and the offset peak are indeed predominantly caused by scatter from the coverglass and photovoltaic layers, respectively, then perhaps the offset specular peak reaches a higher magnitude because the coverglass material properties lead to more reflection and less absorption compared to the photovoltaic material.

Interestingly, when the illumination spot location and metal bar orientation are fixed, the apparent orientation of the diffraction pattern also changes as θ_i increases. In fact, both the diffraction pattern and the offset specular peak measurements seem to compress in the out-of-plane direction. Figures 4(a) and 4(b) demonstrate this phenomenon for one particular illumination spot and solar cell orientation when $\theta_i = 20°$ and $\theta_i = 60°$, respectively. This phenomenon will be addressed within the diffraction model presented in Sec. 4.3.

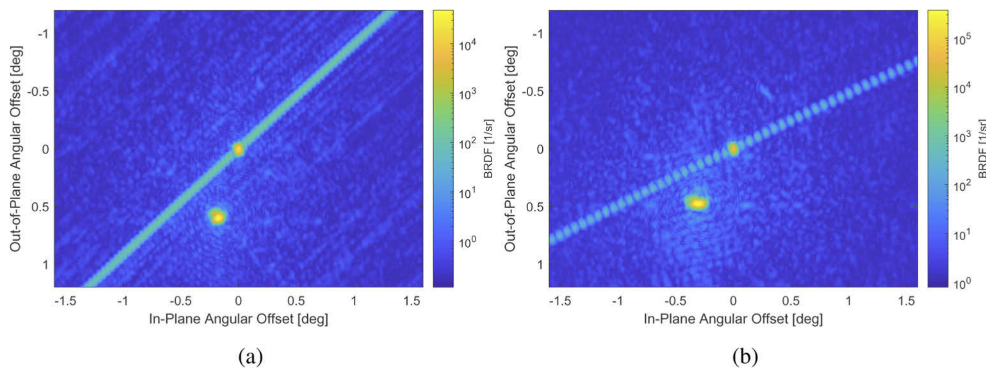

Fig. 4. Solar cell BRDF measurement data using a 15 mW red HeNe laser source with fixed illumination spot and metal bar orientation while varying θ_i from 20° to 60° in (a) and (b), respectively. The apparent diffraction pattern orientation and offset specular peak location shift with θ_i.

Research Article | Vol. 29, No. 22 / 25 Oct 2021 / Optics Express 35507
Optics EXPRESS

3.3. In-plane comparison to CASI

Lastly, with the diffraction pattern oriented in-plane, the original CASI detector was used to validate the CCD measurement. As shown in Fig. 5, using $\theta_i = 40°$ as the example, the agreement is quite good between the industry-standard CASI and the CCD-augmented measurements. The individual diffraction peak spacing matches, and the peak magnitudes measured by the CASI are within the uncertainty range of the CCD measurements [26]. The CASI's maximum measurement uncertainty reaches approximately 17% near the specular direction [28], and so even most conservatively, if that uncertainty value is applied to the entire set of CASI data points, the peak values still fall within the depicted CCD detector uncertainty bounds.

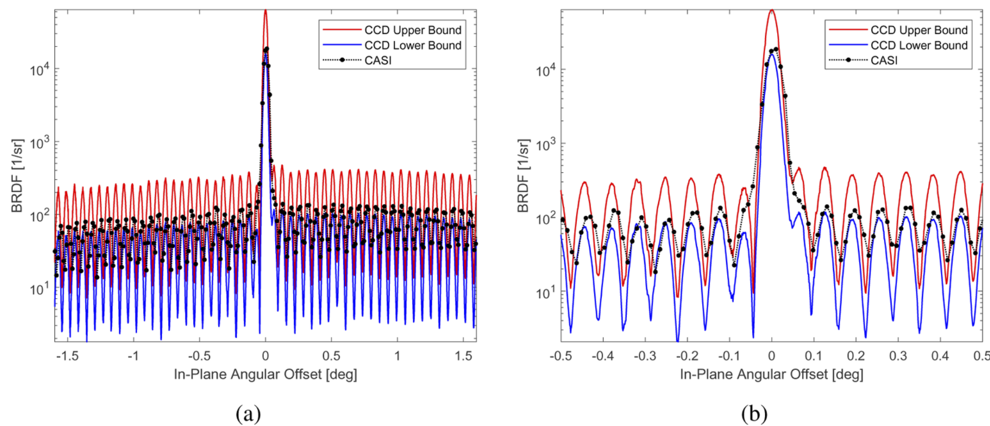

Fig. 5. Comparison of CCD-augmented and original CASI BRDF measurement data with the solar cell diffraction pattern oriented in-plane. The locations and magnitudes of each peak in the CASI measurements agree well with the CCD-augmented measurements and fall within its uncertainty bounds.

Since the traditional CASI detector is constrained to single-pixel slices through the scatter hemisphere, for any other solar cell and diffraction pattern orientation, the CASI is not able to easily measure the out-of-plane diffraction captured by the CCD detector.

4. Solar cell BRDF model

Using the solar cell BRDF measurements from Sec. 3 as the reference, a closed-form BRDF model can be designed with separate terms for each of the three major observed features. The formulations for each term are discussed sequentially below, where f_{r_1}, f_{r_2}, and f_{r_3} represent the center specular peak, offset specular peak, and diffraction pattern, respectively. The full model then becomes the sum $f_{r_1} + f_{r_2} + f_{r_3}$. This approach is similar to many computationally efficient scene-rendering BRDF models, which follow the structure of Eq. (3), and break the model into separate terms which together provide the parameters necessary to fit the overall model to the measured scatter from a particular surface. In this work, overall feature shape and location are emphasized, and so combined numeric results are presented using manual parameter estimates, leaving refined fitting choices for future efforts.

4.1. Center specular peak

The first specular peak, whose center coincides with the center of the diffraction pattern, can be modeled relatively simply by using Eq. (5) with an isotropic Beckmann distribution function to govern peak shape [7,29]. When substituted into Eq. (5), the in-plane specular term can be

written

$$f_{r_1} = \rho_{s_1} \frac{Q(n_1, \hat{\boldsymbol{\omega}}_{\boldsymbol{i}}, \hat{\boldsymbol{\omega}}_{\boldsymbol{s}})}{2(\cos\theta_i + \cos\theta_s)^2} \frac{1}{\pi m_1^2 \cos^4\theta_h} \exp\left[-\frac{\tan^2\theta_h}{m_1^2}\right], \tag{6}$$

which uses only one parameter m_1 to adjust Gaussian peak width. The half-angle θ_h can be calculated for any desired incident and scatter direction combination by implementing Eq. (4). Specific selections for m_1, the weighting parameter ρ_{s_1}, and the complex index of refraction n_1 – which is embedded within Q – are discussed in Sec. 4.4.

4.2. Offset specular peak

The out-of-plane offset specular peak can be modeled using the same basic formulation as the in-plane center peak with Eq. (5). However, the material surface responsible for this peak has a different overall normal direction, which correspondingly impacts the microfacet orientations atop that surface.

One intuitive way to account for this difference is to begin with incident and scatter directions relative to the first surface normal $\hat{\boldsymbol{n}}$, and then rotate each direction in order to express them relative to the second surface normal $\hat{\boldsymbol{n}}_{\boldsymbol{2}}$. This process is very similar to calculating $\hat{\boldsymbol{\omega}}_{\boldsymbol{d}}$ in Eq. (4), and requires finding the rotation that brings $\hat{\boldsymbol{n}}_{\boldsymbol{2}}$ into alignment with $\hat{\boldsymbol{n}}$.

First, the angular offset between $\hat{\boldsymbol{n}}$ and $\hat{\boldsymbol{n}}_{\boldsymbol{2}}$ is described in terms of the parameters $\Delta\theta$ and $\Delta\phi_0$. As shown in Fig. 6(a), $\Delta\theta$ is the difference in zenith angle, defined as a positive value when measured from $\hat{\boldsymbol{n}}$ to $\hat{\boldsymbol{n}}_{\boldsymbol{2}}$, and $\Delta\phi_0$ is the difference in azimuthal angle, defined as a positive value when measured from the $+\hat{x}$ (in-plane forward scatter) direction towards the $+\hat{y}$ (out-of-plane) direction. The arbitrary reference direction $\hat{\boldsymbol{\phi}}_{\text{ref}}$ is used to define the solar cell's orientation about $\hat{\boldsymbol{n}}$, referenced to the -$\hat{x}$ in-plane direction. In this work, $\phi_{\text{ref}} = 0$ when the metal bars are aligned in-plane with the diffraction pattern oriented out-of-plane. For other solar cell orientations, as in Fig. 6(b), ϕ_{ref} is simply added to $\Delta\phi_0$ as an additional azimuthal offset.

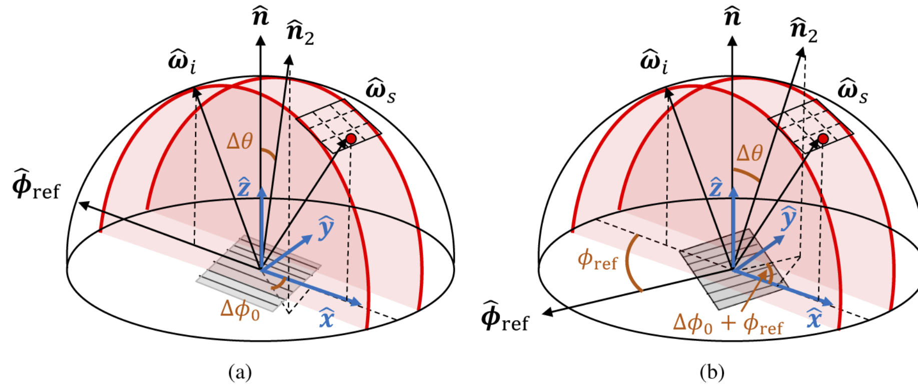

Fig. 6. Illustration of the geometry used to model a specular peak from a second material with a different surface normal direction $\hat{\boldsymbol{n}}_{\boldsymbol{2}}$. The incident and scatter directions $\hat{\boldsymbol{\omega}}_{\boldsymbol{i}}$ and $\hat{\boldsymbol{\omega}}_{\boldsymbol{s}}$ are expressed relative to the first surface normal $\hat{\boldsymbol{n}}$, but can be rotated using the parameters $\Delta\theta$, $\Delta\phi_0$, and ϕ_{ref}, which expresses them relative to the second surface normal $\hat{\boldsymbol{n}}_{\boldsymbol{2}}$ instead. In this graphic, the gray square represents the solar cell surface with metal bar orientation depicted to match $\hat{\boldsymbol{\phi}}_{\text{ref}}$. The red dot within the dashed grid represents an example CCD pixel location, in this case in-plane.

The incident and scatter directions relative to $\hat{\boldsymbol{n}}_{\boldsymbol{2}}$ are then calculated by applying

$$\hat{\boldsymbol{\omega}}_{\boldsymbol{i_2}} = \mathbb{R}_y(-\Delta\theta)\mathbb{R}_z(-\Delta\phi_0 - \phi_{\text{ref}})\hat{\boldsymbol{\omega}}_{\boldsymbol{i}} \tag{7a}$$

$$\hat{\boldsymbol{\omega}}_{\boldsymbol{s_2}} = \mathbb{R}_y(-\Delta\theta)\mathbb{R}_z(-\Delta\phi_0 - \phi_{\text{ref}})\hat{\boldsymbol{\omega}}_{\boldsymbol{s}}, \tag{7b}$$

Optics EXPRESS

which in turn can be used in Eq. (4) to calculate an updated microfacet angle $\hat{\omega}_{h_2}$. Finally, the offset specular peak term can be written

$$f_{r_2} = \rho_{s_2} \frac{Q(n_2, \hat{\omega}_{i_2}, \hat{\omega}_{s_2})}{2(\cos\theta_{i_2} + \cos\theta_{s_2})^2} \frac{1}{\pi m_2^2 \cos^4\theta_{h_2}} \exp\left[-\frac{\tan^2\theta_{h_2}}{m_2^2}\right], \tag{8}$$

which uses the parameter m_2 to adjust Gaussian peak width. As before, specific selections for m_2 as well as the weighting parameter ρ_{s_2} and the complex index of refraction n_2 – which is embedded within Q – are discussed in Sec. 4.4.

4.3. Diffraction pattern

Modeling the diffraction pattern requires a significantly different formulation than the geometric optics-based microfacet terms employed for the center and offset specular peaks. Fortunately, closed-form solutions exist for diffraction through multiple rectangular apertures using Fourier theory with the Fraunhofer approximation [27]. The Fraunhofer conditions apply to the measurements in Sec. 3., based on the highly-focused beam-width (less than 0.15 mm), wavelength of the visible laser source (632.8 nm), and the established distance between sample stage and CCD detector (approximately 0.325 cm) [23].

Fraunhofer diffraction solutions tend to be written in terms of collection plane coordinates, expressed either as linear offsets or angular offsets from an optical axis about which the pattern is centered [27]. For reflection from the solar cell, the diffraction pattern is centered on the specular direction with the $(\bar{x}, \bar{y}, \bar{z})$ coordinate system as shown in Fig. 7. Here, the $\bar{z}$ axis points along the specular direction, and the $\bar{x}$ and $\bar{y}$ axes rotate along with $\hat{\boldsymbol{\phi}}_{\text{ref}}$ to remain aligned with the metal bar orientation. The $\bar{x}$ and $\bar{y}$ directions are chosen so that the projection of $\bar{x}$ aligns longitudinally with the metal bars and the projection of $\bar{y}$ runs transverse to the metal bars.

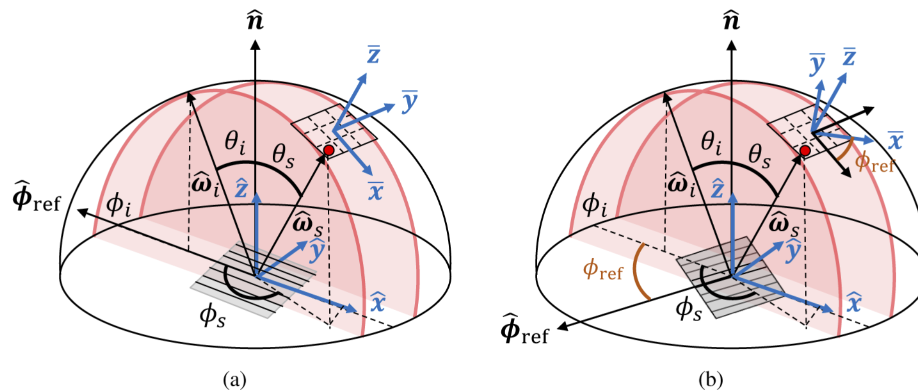

Fig. 7. Illustration of the geometry and coordinates used to model the diffraction pattern under Fraunhofer approximations. The gray square represents the solar cell surface with metal bar orientation depicted to match $\hat{\boldsymbol{\phi}}_{\text{ref}}$. The $\bar{z}$ axis points along the specular direction. When the solar cell is rotated about its normal, denoted by a change in $\hat{\boldsymbol{\phi}}_{\text{ref}}$ from (a) to (b), the $\bar{\boldsymbol{x}}$ and $\bar{\boldsymbol{y}}$ axes also rotate by ϕ_{ref} so that their projections remain aligned with the metal bar orientation. The red dot within the dashed grid represents an example CCD pixel location, in this case with an out-of-plane component.

The best agreement with the measurement results was found by basing the model on the Fraunhofer solution for diffraction through two rectangular stripes with separation a and individual widths b. The pair of stripes can be mathematically represented by a rect function convolved with two delta functions. Since the Fourier transform of a rect is a sinc, and the Fourier transform

Optics EXPRESS

of two delta functions is a cosine, the resulting transverse Fraunhofer irradiance pattern can be represented by $\mathrm{sinc}^2(b\bar{y}/\lambda\bar{z})\cos^2(\pi a\bar{y}/\lambda\bar{z})$ where $\mathrm{sinc}(x) \equiv \sin(\pi x)/\pi x$.

Since the length of each bar extends beyond the effective laser illumination spot, the diffraction pattern is really only a function of the transverse direction $\bar{y}$. However, in practice, the diffraction band does show some tangible width in the $\bar{x}$ direction. The incident laser beam is Gaussian, so simply multiplying by $\exp(-\bar{x}^2/c^2)$ effectively curtails the width of the diffraction band, using c as the Gaussian width parameter.

The Fraunhofer solution so far, however, assumes normal incidence, and when $\bar{y}$ is written in terms of microfacet coordinate angles (shown later in this section), the spacing between modeled diffraction peaks scales with incident angle, contrary to the observations which show consistent spacing for different incident angles. The grating equation, written $\sin\theta_m = m\lambda/a + \sin\theta_i$, demonstrates the potential impact of incident angle on diffraction order spacing. By looking at its derivative, it is possible to see that multiplying the arguments of the sinc^2 and $\cos^2$ functions by $\sqrt{1-\sin^2\theta_i} = \cos(\theta_i)$ should instead preserve consistent spacing as θ_i varies. In practice, an extra factor of two was required, demonstrated by models in Sec. 4.4.2,

Combining the pieces above, the diffraction model can be written in terms of $\bar{x}$, $\bar{y}$, and $\bar{z}$ as

$$f_{r_3} = \rho_{s_3}\cos^2\left(\frac{2\pi a\bar{y}}{\lambda\bar{z}}\cos(\theta_i)\right)\mathrm{sinc}^2\left(\frac{2b\bar{y}}{\lambda\bar{z}}\cos(\theta_i)\right)\exp\left[-\frac{\bar{x}^2}{c^2}\right]. \tag{9}$$

The leading constant ρ_{s_3} is used to adjust the magnitude of the pattern, which would otherwise be normalized to a peak value of one.

BRDFs are ubiquitously written as functions of incident and scatter angles rather than linear coordinates, and so several different formulations were attempted for expressing $\bar{x}$, $\bar{y}$, and $\bar{z}$ in terms of angles. Rather than writing them directly in terms of $\hat{\boldsymbol{\omega}}_{\boldsymbol{s}}$ and $\hat{\boldsymbol{\omega}}_{\boldsymbol{i}}$, the most effective method discovered involves writing them in terms of the half-angle direction $\hat{\boldsymbol{\omega}}_{\boldsymbol{h}}$. Favorably, $\theta_h = 0$ naturally occurs at the specular peak for any θ_i, so that $\bar{x}$ and $\bar{y}$ equal zero there. Good agreement with measurement was achieved by writing

$$\bar{x} = R\sin\theta_h\cos(\phi_h - \phi_{\mathrm{ref}} + \pi) \tag{10a}$$

$$\bar{y} = R\sin\theta_h\sin(\phi_h - \phi_{\mathrm{ref}} + \pi) \tag{10b}$$

$$\bar{z} = R. \tag{10c}$$

The extra π accounts for the convention of measuring ϕ_s and ϕ_h from the -$\hat{x}$ direction [24]. Conveniently, the R cancels out inside both the $\cos^2$ and sinc^2 terms in Eq. (9). Also, in this format, although the $\bar{x}$ and $\bar{y}$ coordinates tend to compress as θ_i increases (due to changes in θ_h), the added $2\cos\theta_i$ within Eq. (9) offsets this impact.

As will be shown in the next section, this choice for the diffraction model and the $(\bar{x}, \bar{y}, \bar{z})$ coordinate conversion sufficiently models the diffraction pattern curvature and orientation changes observed for various θ_i and ϕ_{ref}, matching the measurements in Figs. 2–4.

4.4. Numeric model

This section combines the three BRDF model terms from Secs. 4.1–4.3 and compares them to the measurements from Sec. 3. Numeric model parameters are manually selected based largely on physical material characteristics, rather than using any fitting or optimization algorithms. In order to make valid comparisons, the models are used to generate BRDF results for the same incident and scatter angles which comprise each pixel within the specular CCD measurements. The derivation of those angles are described in previous work [24].

4.4.1. Parameter selection

The in-plane center specular peak model contains three parameters: m_1, n_1 and ρ_{s_1}. After some manual parameter adjustment to qualitatively approximate the specular peak width and magnitude, m_1 and ρ_{s_1} are set for this analysis to 2×10^{-4} and 0.015, respectively. By assuming that scatter mainly from the InGaP layer causes this peak, n_1 can be set to the real component of InGaP's index of refraction, 3.6 at 632.8 nm. [30] Note that in reality, the InGaP actually acts as a diffraction grating because its surface is broken up by the periodic metal bars. However, the ratio of exposed InGaP to metal bar surface is 80:1, so the bulk of the diffraction energy is concentrated on the 0th order. Therefore, only the 0th order peak is modeled here.

The out-of-plane offset specular peak model contains five parameters: m_2, n_2, ρ_{s_2}, $\Delta\theta$, and $\Delta\phi_0$. After some manual parameter adjustment to qualitatively approximate peak width and magnitude, m_2 is set to 2×10^{-4} and ρ_{s_2} is set to 0.7. The coverglass and the space-grade encapsulant used for its adhesion both have real-valued refractive indices of 1.4, so n_2 is set to this value, assuming this peak is caused mainly by scatter from the coverglass. For proof of concept, $\Delta\theta$ and $\Delta\phi_0$ are simply set to 0.5° and 45°, respectively, which should place the location of the offset peak within the CCD detector field of view, but down (in the $+\hat{y}$ out-of-plane direction) and to the right (in the $+\hat{x}$ in-plane direction) of the in-plane peak when $\phi_{\text{ref}} = 0$.

The diffraction pattern model contains four parameters: a, b, c, and ρ_{s_3}. Physically, a represents the spacing between the solar cell's metal bars, which also dictates the separation between high-frequency diffraction peaks according to the quantity $\lambda/a\bar{z}$. Based on the measured vertical pattern spacing from Fig. 2(a) and the CCD's nominal distance from the sample, the derived bar spacing is approximately 7.5×10^{-4} m, which corresponds closely to the product specification. Thus, for this section, a is set to the product specification of 8×10^{-4} m. The parameter b physically represents the width of each metal bar, which is set to the product specification 1×10^{-5} m. Since the ratio of metal bar to total solar cell surface area is only 1:80, the diffracted energy is distributed over many diffraction orders. The parameter ρ_{s_3} is expected to be quite large, as it is associated with the overall reflectance of the metal. It is set to 300 here, so that the normalized $\cos^2$ and sinc^2 functions approximately match the diffraction peak magnitudes. The parameter c is set to 4×10^{-5} to qualitatively set the diffraction pattern width.

4.4.2. Model results and comparison to measurements

Using the numeric parameter values discussed in Sec. 4.4.1, Fig. 8 shows the BRDF model results for incident angles of 20° and 60° with the solar cell's metal bars oriented in-plane ($\phi_{\text{ref}} = 0$) and using scatter angles to match CCD pixel locations during the specular measurements in Fig. 2. Following Fig. 2's format, Figs. 8(a) and 8(c) display the entire modeled pixel array, while Figs. 8(b) and 8(d) extract BRDF values from the pixel columns running vertically (out-of-plane) through the center of each specular peak.

Qualitatively, this model succeeds in reproducing the diffraction pattern and both specular peaks discovered during measurement, and quantitatively, the modeled maximum values of each feature are well within an order of magnitude of the measured values. The modeled center peak is located in the primary specular direction, as desired, with maximum magnitudes of 1.11×10^4 sr^{-1} and 3.91×10^4 sr^{-1} for $\theta_i = 20°$ and 60°, respectively, which compare well to the measured peak values of 9.90×10^3 sr^{-1} and 4.83×10^4 sr^{-1} at those incident angles.

The modeled offset peak has shifted down and to the right, as expected, and includes a slight compression of the down (or out-of-plane) component at the higher incident angles. This peak's maximum values are approximately 4.44×10^4 sr^{-1} and 4.19×10^5 sr^{-1} for $\theta_i = 20°$ and 60°, respectively, which compare well to the measured peak values of 6.03×10^4 sr^{-1} and 4.21×10^5 sr^{-1} at those incident angles.

At higher incident angles, the curve noticeable in the measurements is also noticeable in the model. The modeled diffraction peak magnitudes range from 300 sr^{-1} nearest the center specular

Optics EXPRESS

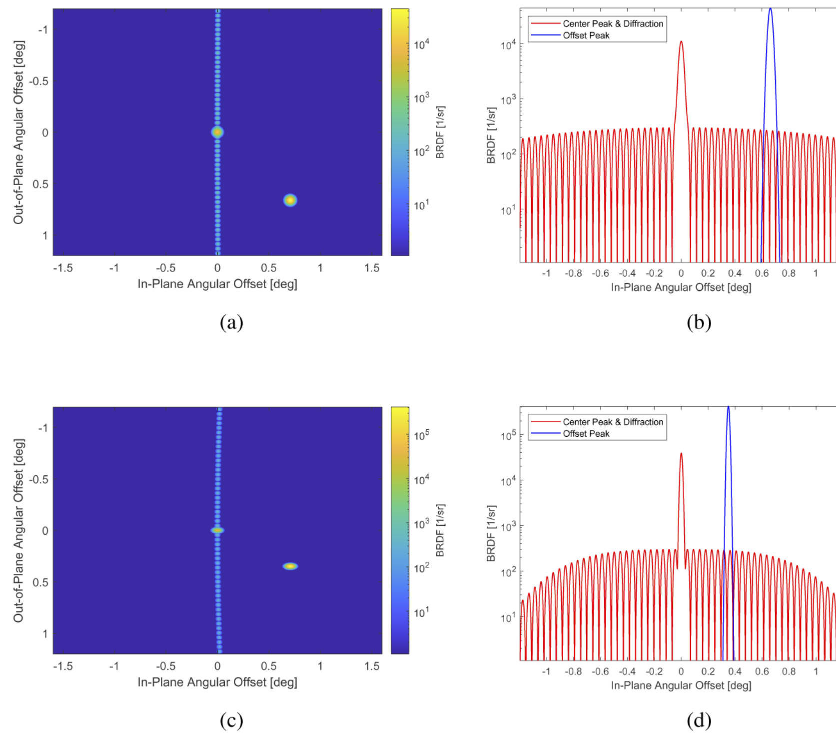

Fig. 8. Combined solar cell BRDF model results with in-plane metal bar orientation. The scatter coordinates are the same as the CCD pixel coordinates measured in Fig. 2, with $\theta_i = 20°$ in (a) and (b), and $\theta_i = 60°$ in (c) and (d). The full pixel arrays are modeled in (a) and (c), with vertical pixel columns through the center of each peak plotted in (b) and (d). The model successfully replicates each of the three primary measured features (center specular peak, offset specular peak, and diffraction pattern), and the peak values for each modeled feature compare to the measured data well within an order of magnitude.

peak to 209 sr^{-1} at each edge of the array. By comparison, when $\theta_i = 20°$, the peak measured diffraction value near the center is 312 sr^{-1} while the peak values nearest each edge average to 145 sr^{-1}. When $\theta_i = 60°$, the peak measured diffraction value near the center is 312 sr^{-1} while the peak values nearest each edge average to 202 sr^{-1}. Particularly at $\theta_i = 60°$, the vertical pixel slice in Fig. 8(d) no longer follows the diffraction peaks as closely, so the peak values are artificially reduced near the edges.

Since the metal bar separation is only known to one significant figure (800 μm), the modeled diffraction peak spacing also agrees well with the measured diffraction peak spacing (within 8%). For both incident angles, there are 26 modeled peaks between the CCD center and edges, and 24.5 measured peaks between the center and edges. It is worth noting that omitting the $2\cos\theta_i$ within Eq. (9) – whose inclusion was motivated by the grating equation described in Sec. 4.3 – changes the modeled diffraction pattern spacing so that 14 modeled peaks exist between the CCD center and edge when $\theta_i = 20°$ compared to 26 modeled peaks when $\theta_i = 60°$.

Changing the value of ϕ_{ref} models changing the metal bar orientation relative to the plane of incidence. Figures 9(a) and 9(b) show that by setting $\phi_{\text{ref}} = 45°$ and 90°, respectively, the modeled diffraction pattern and offset peak both rotate about the central peak, mimicking the measured behavior in Fig. 3. In addition, Figs. 10(a) and 10(b) show that for a fixed metal bar orientation – for example $\phi_{\text{ref}} = 45°$ – the apparent orientation of the diffraction pattern changes as θ_i increases, mimicking the measured behavior in Fig. 4. Here, it is important to note that

Optics EXPRESS

without writing $\bar{x}$, $\bar{y}$, and $\bar{z}$ in terms of $\hat{\omega}_h$ in Eq. (10), the model would fail to account for these observed phenomena; therefore, the model is written in terms of $\hat{\omega}_h$.

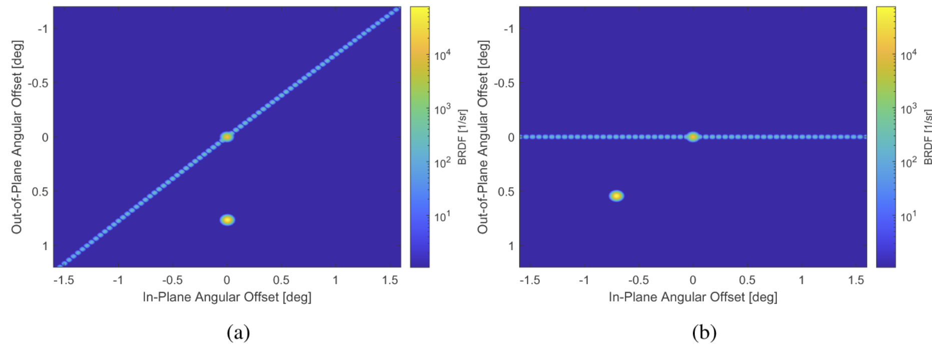

Fig. 9. Combined solar cell BRDF model results with metal bars oriented (a) 45° out-of-plane and (b) 90° out-of-plane. The scatter coordinates are the same as the CCD pixel coordinates measured in Fig. 3 with $\theta_i = 40°$. As in the measured results, the offset specular peak and diffraction pattern rotate about the center specular peak.

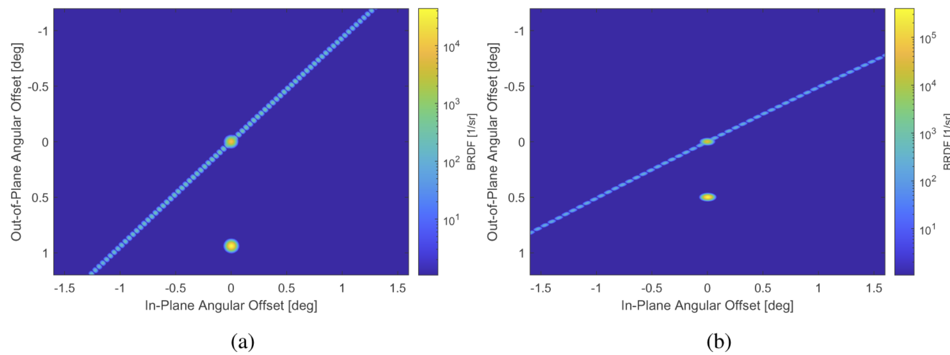

Fig. 10. Combined solar cell BRDF model results while varying θ_i from 20° to 60° in (a) and (b). The scatter coordinates are the same as the CCD pixel coordinates in Fig. 4 and $\phi_{\text{ref}} = 45°$. Similar to the measured results, the out-of-plane components compress as θ_i increases, altering the apparent orientation of the diffraction pattern.

5. Conclusion

This paper presented BRDF measurement results for a commercially available solar cell designed for satellites. A CCD-augmented CASI was used to capture in-plane and out-of-plane BRDF data with high spatial resolution for various incident angles. The data showed three distinct scatter features: 1) one central specular peak, 2) another specular peak offset from the first, and 3) a diffraction pattern. The specular peaks appeared to originate from two distinct material surfaces with slightly different normal directions, and the diffraction pattern was caused by metal conducting bars periodically spaced in one direction across the solar cell. A traditional CASI detector was used to validate the central peak and diffraction pattern with in-plane measurements.

The measurements were used to inform the creation of a single closed-form model to capture the functionality of each BRDF feature. The central specular peak term was modeled using a common microfacet formulation. The offset specular peak term used a similar formulation, but required rotating the incident and scatter directions to account for the difference in surface

Optics EXPRESS

normal direction. Finally, the diffraction pattern term was based on the closed-form solution for diffraction through two rectangular apertures using the Fraunhofer approximation, adjusted and written in terms of microfacet coordinates. Parameters for each term were chosen based on physical material properties, rather than using optimized fitting algorithms.

Model results were compared to the measurements by using the same CCD pixel scatter coordinates. The solar cell BRDF model successfully replicated each feature. As the solar cell's metal bar orientation is rotated relative to the in-plane direction, both the offset specular peak location and diffraction pattern orientation rotate in kind. In addition, as incident angle increases, the out-of-plane components compress, leading to apparent differences in offset peak location and diffraction pattern orientation and curvature. Quantitatively, the peak values of each model feature agree with the measurements well within an order of magnitude, and the diffraction pattern spacing remains consistent across various incident angles.

Ultimately, this work outlines a process for using high-spatial-resolution BRDF measurements to inform the creation of new BRDF models capable of describing out-of-plane specular features. Although applied to a solar cell here, a similar process can be applied to other materials. The resulting models can later be incorporated into a variety of radiometric simulations or scene generators in hopes of improving the accuracy of predicted observations.

Funding. Air Force Office of Scientific Research (F4FGA09014J002).

Disclosures. The authors declare no conflicts of interest.

Data availability. Data underlying the results presented in this paper are not publicly available at this time but may be obtained from the authors upon reasonable request.

References

1. F. Nicodemus, J. Richmond, J. Hsia, I. Ginsberg, and T. Limperis, "Geometric Considerations and Nomenclature for Reflectance," National Bureau of Standards Monograph 160, Department of Commerce (1977).
2. B. Sandford and L. Robertson, "Infrared reflectance properties of aircraft paint," in *IRIS Targets, Backgrounds, and Discrimination*, (1985).
3. D. Wellems, S. Ortega, D. Bowers, J. Boger, and M. Fetrow, "Long wave infrared polarimetric model: theory, measurements, and parameters," J. Opt. A: Pure Appl. Opt. **8**(10), 914–925 (2006).
4. J. Conant and F. Iannarilli Jr., "Development of a combined bidirectional reflectance and directional emittance model for polarization modeling," Proc. SPIE **4481**, 206–215 (2002).
5. F. Nicodemus, "Directional reflectance and emissivity of an opaque surface," Appl. Opt. **4**(7), 767–773 (1965).
6. J. T. Kajiya, "The rendering equation," SIGGRAPH Comput. Graph. **20**(4), 143–150 (1986).
7. K. Torrance and E. Sparrow, "Theory for off-specular reflection from roughened surfaces," J. Opt. Soc. Am. **57**(9), 1105–1114 (1967).
8. S. Butler and M. Marciniak, "Robust categorization of microfacet BRDF models to enable flexible application-specific BRDF adaptation," Proc. SPIE **9205**, 920506 (2014).
9. S. Rusinkiewicz, "A new change of variables for efficient BRDF representation," in *Rendering Techniques '98*, (1998), pp. 11–22.
10. J. Harvey, A. Krywonos, and C. Vernold, "Modified Beckmann-Kirchhoff scattering model for rough surfaces with large incident and scattering angles," Opt. Eng. **46**(7), 078002 (2007).
11. J. Harvey, A. Krywonos, and J. Stover, "Unified scatter model for rough surfaces at large incident and scatter angles," Proc. SPIE **6672**, 66720C (2007).
12. A. Krywonos, J. Harvey, and N. Choi, "Linear systems formulation of scattering theory for rough surfaces with arbitrary incident and scattering angles," J. Opt. Soc. Am. A **28**(6), 1121–1138 (2011).
13. S. Butler, S. Nauyoks, and M. Marciniak, "Comparison of microfacet BRDF model to modified Beckmann-Kirchhoff BRDF model for rough and smooth surfaces," Opt. Express **23**(22), 29100–29112 (2015).
14. B. Ewing, S. Butler, and M. Marciniak, "Improved grazing angle bidirectional reflectance distribution function model using Rayleigh–Rice polarization factor and adaptive microfacet distribution Function," Opt. Eng. **57**(10), 1–9 (2018).
15. J. Filip, R. Vavra, and M. Havlicek, "Effective acquisition of dense anisotropic BRDF," *Proceedings of the 22nd International Conference on Pattern Recognition* pp. 2047–2052 (2014).
16. W. Matusik, H. Pfister, M. Brand, and L. McMillan, "A data-driven reflectance model," ACM Trans. Graph. **22**(3), 759–769 (2003).
17. H. Wang, W. Zhang, and A. Dong, "Modeling and validation of photometric characteristics of space targets oriented to space-based observation," Appl. Opt. **51**(32), 7810–7819 (2012).

18. D. Bowers, D. Wellems, M. Duggin, W. Glass, and L. Vaughan, "Broadband spectral-polarimetric BRDF scan system and data for spacecraft materials," in *Advanced Maui Optical and Space Surveillance Technologies Conference*, (2011).
19. A. Ceniceros, D. Gaylor, J. Anderson, E. Pinon, P. Dao, and R. Rast, "Comparison of BRDF-predicted and observed light curves of GEO satellites," in *Advanced Maui Optical and Space Surveillance Technologies Conference*, (2015).
20. M. Duggin, J. Riker, W. Glass, K. Bush, D. Briscoe, M. Klein, M. Pugh, and B. Engberg, "Multi-spectral image analysis for improved space object characterization," in *Advanced Maui Optical and Space Surveillance Technologies Conference*, (2008).
21. T. Kelecy and M. Skinner, "Non-imaging characterization assessment of shedding events from derelict satellites near geosynchronous orbit (GEO)," in *Advanced Maui Optical and Space Surveillance Technologies Conference* (2016).
22. R. Cognion, "Observations and modeling of GEO satellites at large phase angles," in *Advanced Maui Optical and Space Surveillance Technologies Conference* (2013).
23. T. Small, S. Butler, and M. Marciniak, "Augmenting CASI BRDF measurement device to measure out-of-plane scatter with CCD pixel array," Proc. SPIE **11485**, 114850B (2020).
24. T. Small, S. Butler, and M. Marciniak, "Scatter Coordinate mapping and out-of-plane BRDF measurements for specular materials using an augmented CASI measurement system," Proc. SPIE **11727**, 117270X (2021).
25. G. Olsen, M. Ettenberg, and R. D'Aiello, "Vapor-grown InGaP/GaAs solar cells," Appl. Phys. Lett. **33**(7), 606–608 (1978).
26. T. Small, S. Butler, and M. Marciniak, "Uncertainty analysis for CCD-Augmented CASI BRDF measurement system," Submitted to Optical Engineering on 7 Jun 2021.
27. J. Goodman, *Introduction to Fourier Optics*, 4th Ed. (W.H. Freeman, 2017).
28. S. Butler, S. Nauyoks, and M. Marciniak, "Experimental measurement and analysis of wavelength-dependent properties of the BRDF," Proc. SPIE **9611**, 96110G (2015).
29. P. Beckmann and A. Spizzichino, *The Scattering of Electromagnetic Waves from Rough Surfaces* (MacMillan, 1963).
30. M. Schubert, V. Gottschalch, C. Herzinger, H. Yao, P. Snyder, and J. Woollam, "Optical constants of $Ga_xIn_{1-x}P$ lattice matched to GaAs," J. Appl. Phys. **77**(7), 3416–3419 (1995).